Available online at www.sciencedirect.com
ScienceDirect
International Journal of Heat and Fluid Flow 29 (2008) 874–890
International Journal of HEAT AND FLUID FLOW
www.elsevier.com/locate/ijhff

Experimental transport-rate budgets in complex 3-D turbulent flow near a wing/body junction

Semih M. Ölçmen [a,*], Roger L. Simpson [b]

[a] Aerospace Engineering and Mechanics Department, The University of Alabama, Tuscaloosa, AL 35487, United States
[b] Aerospace and Ocean Engineering Department, Virginia Tech, Blacksburg, VA 24061, United States

Received 5 July 2007; received in revised form 14 December 2007; accepted 17 December 2007
Available online 11 February 2008

Abstract

Experimental flow measurements are presented for a wing–body junction flow obtained using laser-Doppler velocimetry. Mean velocity and Reynolds stress data are used to calculate the complete transport-rate budgets of Reynolds stresses and turbulent kinetic energy. The measurements were carried out in the Virginia Tech Boundary Layer Tunnel at a nominal air speed of 27.5 m/s around a NACA 0020 tail and 3:2 elliptical nose wing shape. Data are presented for a two-dimensional turbulent boundary layer (2DTBL), a strongly skewed three-dimensional turbulent boundary layer (3DTBL), a location in the vicinity of a 3-D separation line, and around the center of the vortex in the horse-shoe vortex that forms around the wing. Terms in the transport-rate equations were calculated also using the measured triple order fluctuating velocity products. Results show that the pressure-diffusion approximated by Lumley [Lumley, J.L., 1978. Computation modeling of turbulent flows. Adv. Appl. Mech. 18, 124–176] is an important term in the balance of $\overline{v^2}$, $\overline{uv}$, and $\overline{vw}$ stress budgets; there were distinct differences between the two-dimensional and three-dimensional turbulent boundary layer budgets. Qualitative comparisons of experimental stress-transport-rate budgets to previous DNS results show a better agreement using the anisotropic dissipation rate of Hallbäck et al. [Hallbäck, M., Groth, J., Johansson, A.V., 1990. An algebraic model for nonisotropic turbulent dissipation rate in Reynolds stress closure, october. Phys. Fluids A 2 (10), 1859–1866].

Keywords: Turbulence; Wing/body junction flow; Three-dimensional boundary layer; Laser-Doppler velocimeter

1. Introduction

In the present work a term-by-term investigation of the transport-rate budgets is presented using experimental data for a 2DTBL flow and for a complex wing–body junction 3DTBL flow (Ölçmen and Simpson, 1996b,c). Mean velocity, shear stress, triple order and fourth order product data obtained at locations with different flow complexity are used to calculate the terms in the Reynolds stress transport equations (Launder et al., 1975) together with the pressure-diffusion model of Lumley (1978) and the anisotropic dissipation rate model of Hallbäck et al. (1990). Each term was determined using only the experimental data in order to present purely experimental values for the terms. This work, therefore, provides a transport-rate budget analysis that can be employed for Reynolds stress turbulence-modeling in complex flows.

In a wing–body junction flow the approach boundary layer on the wall upstream of the wing separates from the wall due to the pressure gradients generated by the presence of the wing, and rolls inwards to the wing/wall junction to generate an unsteady vortical structure in the vicinity of the nose of the wing (Fig. 1). The vortical structure forming at the nose region is stretched around the wing to generate a vortical structure named as the "horse-shoe vortex". The data used here are portion of a set of measurements made in the horse-shoe vortex. Fig. 1 shows the schematic of the wing–body junction and the measurement locations

* Corresponding author. Tel.: +1 205 348 4003.
E-mail addresses: solcmen@eng.ua.edu (S.M. Ölçmen), simpson@aoe.vt.edu (R.L. Simpson).

0142-727X/$ - see front matter © 2007 Elsevier Inc. All rights reserved.
doi:10.1016/j.ijheatfluidflow.2007.12.004

Nomenclature

C_p static pressure coefficient
$(\partial C_p/\partial x)_{FS}$ static pressure coefficient gradient
C_{ij} convection tensor
$FA = \arctan(W/U)$ flow angle
$FGA = \arctan\left(\frac{\partial W/\partial y}{\partial U/\partial y}\right)$ flow-gradient angle
p fluctuating pressure component
PR_{ij} production tensor
PD_{ij} pressure-diffusion tensor
Re_θ Reynolds number based on momentum thickness
$SSA = \arctan(\frac{\overline{vw}}{\overline{uv}})$ shear stress angle
t wing maximum thickness, $t = 7.17$ cm
TD_{ij} turbulent diffusion tensor
$TKE = k = (\overline{u_i u_i})/2$ turbulent kinetic energy
U_e velocity magnitude at the boundary layer edge
U_i mean velocity components
$\overline{u_i u_j}$ Reynolds stress tensor, $i = 1, 2, 3$; $j = 1, 2, 3$
$\overline{u_i u_j u_k}$ triple velocity correlation tensor
$U^+ = \frac{U}{u_\tau}$ non-dimensional mean velocity
$u_\tau = \sqrt{\tau_w/\rho}$ skin-friction velocity
VD_{ij} viscous diffusion tensor
x_{TC}, y_{TC}, z_{TC} tunnel coordinates
$y^+ = yu_\tau/\nu$ wall-law variable
β_{FS} flow angle at the boundary layer edge
β_{WC} wall-stress direction
δ_{ij} Dirac delta function, $\delta_{ij} = 1$ if $i = j$, $\delta_{ij} = 0$ if $i = j$
δ boundary layer thickness
ε_{ij} viscous dissipation tensor
$\varepsilon = \varepsilon_{ii}/2$ dissipation of turbulent kinetic energy
$\theta = \int_0^\infty \left(1 - \frac{U}{U_e}\right)\frac{U}{U_e}\,dy$ momentum thickness
ν kinematic viscosity
ρ density
σ standard deviation
$\tau = \sqrt{(-\rho\overline{uv})^2 + (-\rho\overline{vw})^2}$ shear stress magnitude in the flow
τ_w wall shear stress
Φ_{ij} pressure–strain tensor

used in the current paper. The wing used is a 3:2 elliptical nosed, NACA 0020 tailed wing profile with maximum thickness of 7.17 cm, chord length of 30 cm, and a height of 22 cm. It was mounted perpendicular to the flat bottom surface of the Boundary Layer Tunnel with a (0.91 m × 0.254 m) rectangular cross section and 8 m long tunnel test section. The nominal air speed was 27.5 m/sec resulting in a Re_θ of the flow at 0.75 chord upstream of the wing equal to 5936. Conditions of the present flow field are well documented (Simpson, 1996). The approach flow conditions, surface oil flows, and wall static pressure distribution were previously presented (Ölçmen, 1990; Ölçmen and Simpson, 1995a; and Simpson, 2001). Ailinger (1990) measured the surface skin-friction at selected locations using oil-film interferometry.

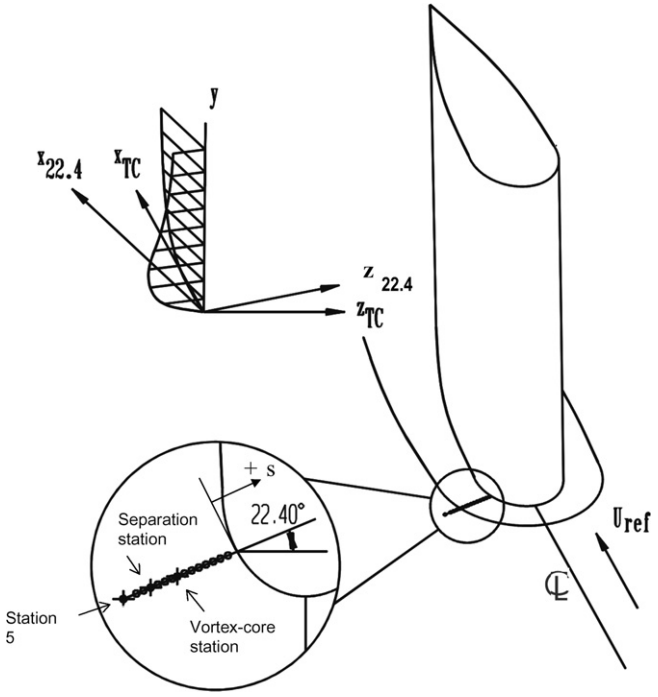

Fig. 1. Schematic view of the wing and the measurement locations, and description of the coordinate systems. $(\,)_{22.4}$, wing-perpendicular coordinates, $(\,)_{TC}$, tunnel coordinates.

Wing–body junction separated vortical flows have been studied extensively by Simpson's group at Virginia Tech (Simpson, 1996, 2001; Devenport and Simpson, 1990, 1992; Shinpaugh and Simpson, 1995; Ölçmen, 1990; Ölçmen and Simpson, 1994, 1995a,b, 1996a,b,c,d,e; Fleming et al., 1993, 1995; Ha and Simpson, 1993; Lewis et al., 1994; Kim et al., 1991). This flow field has been used as a computational test case, e.g. (Sung and Yang, 1998; Bonnin et al., 1996; Parneix et al., 1998; Deng and Visonneau, 1999; Apsley and Leschziner, 2001), using more than thirteen turbulence closure models ranging from an isotropic eddy-viscosity model to versions of the k–ε model and Reynolds stress models. Results showed that all the codes underpredicted the strength and size of the vortex around the wing and near the nose region, as well as the TKE values within the separation vortex that forms near the nose region. Conversely, the TKE values near the stagnation region were overpredicted. These results were attributed to the modeling of terms in Reynolds stress models indicating the need for further data in such complex flows.

A recent paper by Ölçmen and Simpson (2006) and its cited references discuss the details of the flow field with a special emphasis on the flow field within the horse-shoe vortex to the side of the wing. In that paper thirty eight closely spaced velocity profiles were used to investigate the physics within the horse-shoe vortex. Fig. 2 shows the mean velocity magnitude and the secondary flow streamlines in the plane perpendicular to the floor and passing through the 22.4° line. The abscissa shows the distance from the wing where the wing is located at $s = 0$, and the ordinate is logarithmically spaced. Fig. 2 shows that a large vortex is located in the outer region and entrains the high speed free-stream flow close to the wall, especially close to the wing. At $s \approx -4.2$ cm the flow experiences a three-dimensional separation where all the secondary streamlines merge towards a point. At distances closer to the wing ($s \approx -0.4$ cm), the flow direction is reversed (Fig. 2). The results showed that the normal and shear stresses within the horse-shoe vortex are an order of magnitude larger compared to values measured in a three-dimensional boundary layer just outside the junction vortex. Bimodal histograms of the w fluctuating velocity were measured under the outer layer vortex near the wall due to the time-dependent chaotic nature of the horse-shoe vortex. It was also observed that the shear–stress angle (SSA) highly lags the flow-gradient angle (FGA), and the turbulence diffusion is highly altered due to the presence of vortical structures.

Measurements used in this paper are the data obtained at selected locations. The locations selected are Station 5, Separation, and Vortex-core stations (Fig. 2). Plots of the measured profiles in a plane perpendicular to the tunnel floor encompassing the measurement station locations show that the Separation and Vortex-core stations correspond to the location where the 3DTBL goes through a 3-D separation and to the location where the center of the outer region vortex is located, respectively. Station 5 data were chosen since the data are for a 3DTBL just outside the horse-shoe vortex. Additional measurements made on a line 3.175 mm downstream of the 22.4° line at these selected locations were also used to calculate the axial gradients of the variables. Two-dimensional TBL profiles were obtained at the same Reynolds number flow without the presence of the wing to serve as a baseline in comparison.

The data and the following discussions are presented in tunnel coordinates throughout the paper. Fig. 1 shows the coordinate system definitions. The $()_{22.4^\circ}$ stands for the wing-perpendicular coordinates and the $()_{TC}$ stands for the tunnel coordinates. The y axis is perpendicular to the floor. Positive x_{TC} is along the tunnel axis looking downstream with its origin at the wing-floor intersection. Positive $x_{22.4^\circ}$ makes 22.4° counter-clockwise with respect to the x_{TC}. The z axes complete right-handed coordinate systems.

In the following sections the mean velocity and the Reynolds stress profiles obtained at the selected stations are discussed. This discussion is followed by the presentation of the transport-rate budget equations and the discussion of the approximations made to extract each term within the transport-rate equations. Next, the transport-rate budgets of the Reynolds stresses as well as the turbulent kinetic energy obtained at the selected stations are comparatively discussed.

2. Mean velocity and shear–stress data at selected stations

In this section a summary of the observations made about the mean velocities and stresses obtained at the above mentioned stations are presented for completeness of the paper. A more detailed discussion on the velocity field can be found in papers by Ölçmen and Simpson (1995a,b, 1996d, 2006). Measurement conditions are given in Table 1. Some length

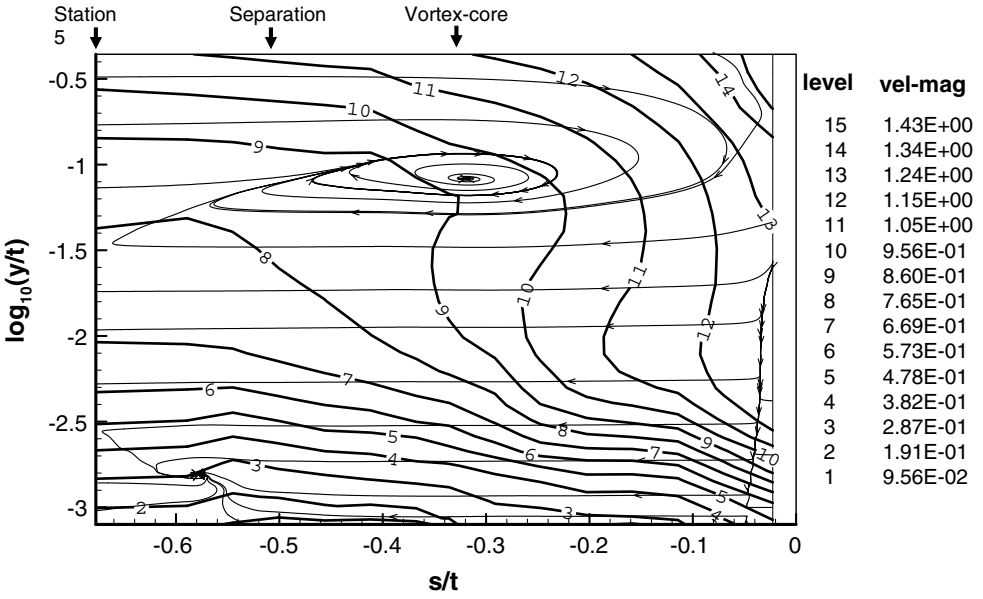

Fig. 2. Velocity magnitude contours and secondary flow streamlines measured at stations along the 22.4° line. Station locations are shown above the figure.

Table 1
Laser-doppler velocimeter locations and flow parameters

Stations	X (mm)	Z (cm)	s/t	U_{ref} (m/sec)	U_e (m/sec)	β_{FS} (°)	β_w (°)	u_τ (m/sec)	v (m^2/sec) x1E05	$(\partial C_p/\partial x)_{FS}$ (1/m)	$(\partial C_p/\partial z)_{FS}$ (1/m)	Daily pressure (millibar)	Daily temperature (°C)
2-D	–	–	–	27.4	27.2	0	0	0.98	1.67	0	0	941.2	24
Station 5	6.6	−7.47	−0.675	27.5	29.2	−7.71	−19.7	1.15	1.64	−6.25	−1.95	945.05	23
Separation	11.18	−6.35	−0.501	27.6	30.2	−10.38	−23.6	1.048	1.68	−8.92	−4.92	935.3	24
Vortex-core	15.75	−5.26	−0.336	27.5	32.3	−13.11	−29.47	1.33	1.67	−12.33	−7.93	941.3	24.8

Pressure coefficient gradients are calculated from the measured pressure distribution. U_e = velocity magnitude at the layer edge. The $(\,)_{FS}$ stands for the free-stream coordinates. Positive x_{FS} is in the direction of the mean velocity direction at the edge of the boundary layer. Y axis is perpendicular to the floor and, z axis completes a right-handed coordinate system.

scales obtained at these stations and the uncertainties in the measured quantities can be found in the report by Ölçmen and Simpson (1996d). Skin-friction values used in non-dimensionalizing the measured quantities were determined in different fashions at different stations. The U/u_τ mean velocity profile at the 2-D station was used to calculate the skin-friction coefficient at the wall using Coles law of the wall ($U^+ = \frac{1}{0.41}\ln(y^+) + 5$, Coles, 1956) (Fig. 3). At Station 5 the skin-friction was measured using an oil-film interferometer (Ailinger, 1990). Skin-friction values at other stations were calculated using the measured mean velocity and the theoretical variations of the mean velocity very near the wall (Ölçmen and Simpson, 2006).

2.1. Mean velocities

The non-dimensional velocity profiles show that (Fig. 3) both at Station 5 and the Vortex-core station the U/u_τ profiles have a greater velocity deficit above $y^+ \approx 50$ in comparison to the 2-D velocity profile. At the Separation station both the velocity gradients near the wall and non-dimensional velocity attain higher values in comparison to the 2-D profile. At the Vortex-core station in the region $y^+ \approx 50$–200 the U/u_τ velocity gradient is approximately zero indicating that the spanwise vorticity component is practically zero in that zone.

The V/u_τ velocities are not affected by the coordinate system rotation (Fig. 3). At the 2-D station velocities increase towards the layer edge. At Station 5, a peak forms at $y^+ \approx 500$. At the Separation and the Vortex-core stations V/u_τ changes sign indicating the direction change for the V component induced by the large-vortical structure (Ölçmen and Simpson, 2006); the magnitude is increased towards the Vortex-core station.

The W/u_τ at 2-D station is very close to zero as expected (Fig. 3). The velocity magnitude peak increases and shifts away from the wall, progressing towards the Vortex-core station with increased three-dimensionality.

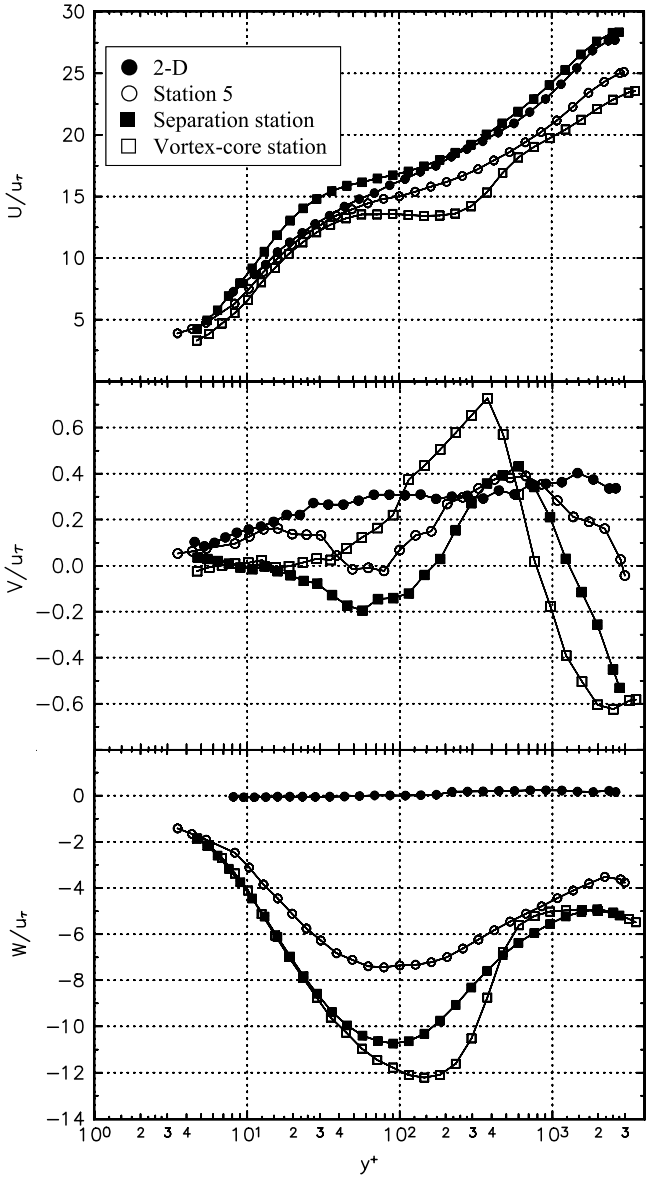

Fig. 3. U/u_τ, V/u_τ, W/u_τ mean velocity at different stations in tunnel coordinates. ●, 2-D; ○, Station ■, Separation station; □, Vortex-core station.

2.2. Normal stresses

Normal stress distributions show that (Fig. 4) the presence of the large outer layer vortical structure results in large velocity fluctuations, at the Vortex-core station. While the $\overline{u^2}/u_\tau^2$ is twice that obtained at Station 5 at the peak location, the $\overline{v^2}/u_\tau^2$ is more than seven times and the $\overline{w^2}/u_\tau^2$ is more than six times compared to both 2-D and

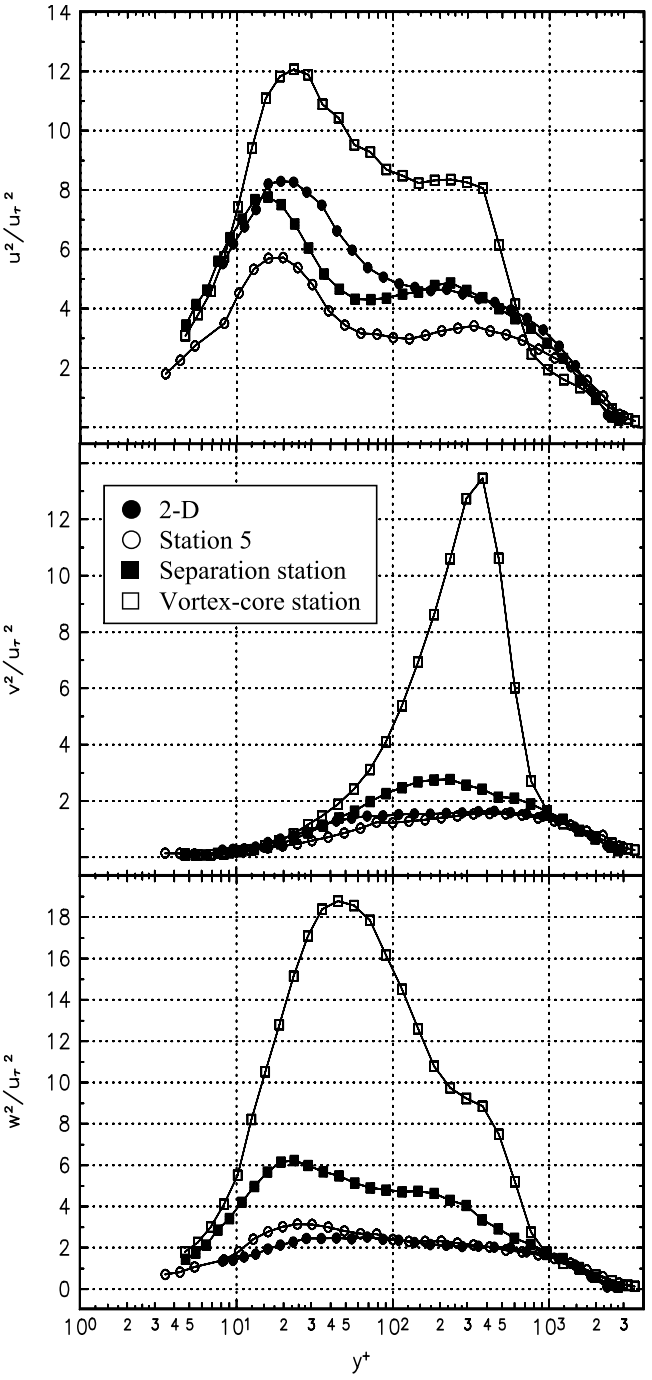

Fig. 4. $\overline{u^2}/u_\tau^2, \overline{v^2}/u_\tau^2, \overline{w^2}/u_\tau^2$ normal stress components at different stations in tunnel coordinates. ●, 2-D; ○, Station 5; ■, Separation station; □, Vortex-core station.

the Station 5 values. An increase in the $\overline{u^2}/u_\tau^2$ was observed due to the bimodal variations observed in the lateral velocity. The $\overline{v^2}/u_\tau^2$ fluctuations were observed due to the meandering and up and down movement of the outer layer vortical structure (Ölçmen and Simpson, 2006). Profiles also show that the Station 5 values are half that of the 2-D station values near the wall ($y^+ \approx 20$) for $\overline{u^2}/u_\tau^2$, although $\overline{v^2}/u_\tau^2$ and $\overline{v^2}/u_\tau^2$ are comparable to each other. At the Separation station while the $\overline{u^2}/u_\tau^2$ values are reduced in the $y^+ \approx$ 15–150 range, the $\overline{v^2}/u_\tau^2$ profile shows an increase between $y^+ \approx$ 50–1000 and $\overline{v^2}/u_\tau^2$ is doubled below $y^+ \approx 1000$. The $\overline{u^2}/u_\tau^2$ reduction near the wall at these stations is presumably due to the ejections by the spanwise vortices (with the rotation opposite to that of the mean flow) being disrupted due to the three-dimensionality of the flow (Compton and Eaton, 1997; Itoh and Kobayashi, 2000), or due to the change in the structure of the near wall flow (Flack, 1997).

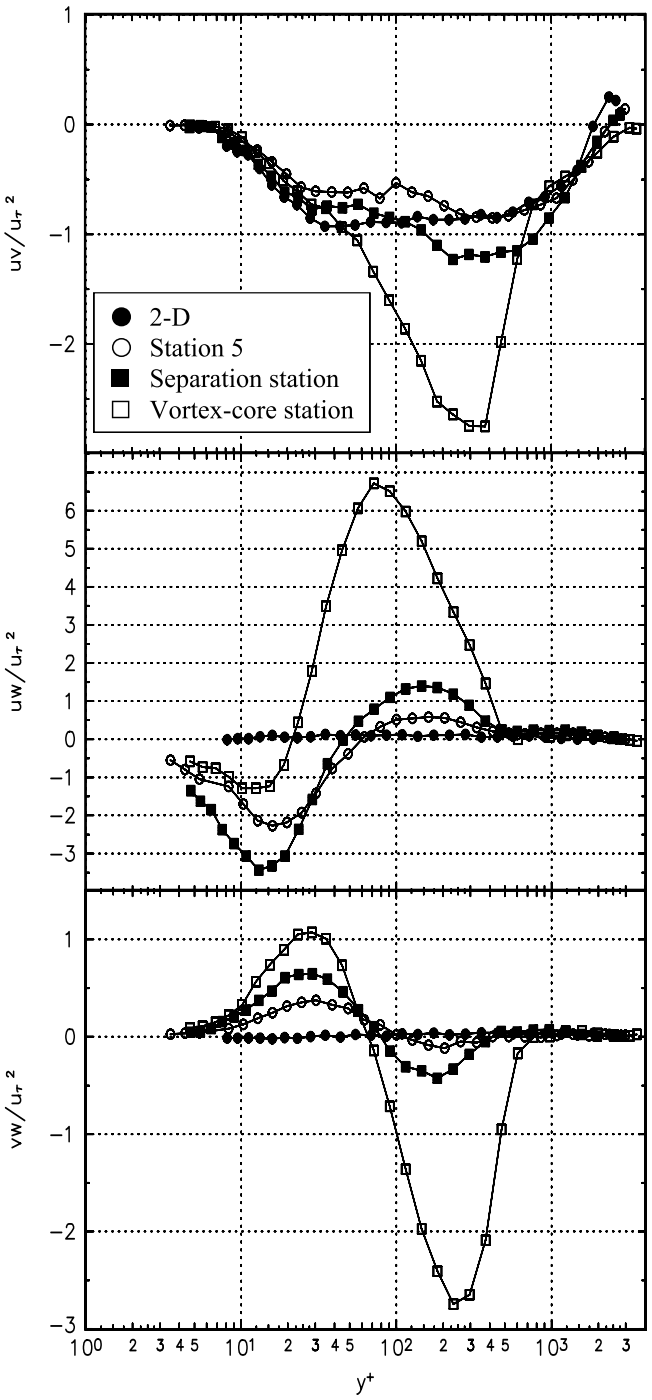

Fig. 5. $\overline{uv}/u_\tau^2, \overline{uw}/u_\tau^2, \overline{vw}/u_\tau^2$ shear stress components at different stations in tunnel coordinates. ●, 2-D; ○, Station 5; ■, Separation station; □, Vortex-core station.

2.3. Shear stresses

At Station 5 and at the Separation station, $\overline{uv}/u_\tau^2$ near wall values below $y^+ \approx 300$ and below $y^+ \approx 100$ are lower than the 2-D values, respectively (Fig. 5), presumably due to the same reason why $\overline{u^2}/u_\tau^2$ is reduced. At the Separation station above $y^+ \approx 100$, the values are higher than the 2-D case. Vortex-core station values peak at $y^+ \approx 400$ with a value ≈3 times higher than the 2-D values. At the Separation and the Vortex-core stations the flow behaves different than a mildly skewed 3-D flow due to the effects of the large-vortical structure on the flow.

The $\overline{uw}$ $\overline{vw}$ shear stresses in a 2-D TBL are nominally zero. The location in the 3-D flow profiles where $\overline{uw}/u_\tau^2$ is zero shifts towards the wall, progressing towards the Vortex-core station (Fig. 5). The positive peak value at the Vortex-core station is an order of magnitude larger than the Station 5 peak value. Above $y^+ \approx 500$ the stress values are very close to zero, showing that the $\overline{uw}/u_\tau^2$ stress in this region is not affected by the near wall structure.

Similarly, $\overline{vw}$ stresses are also close to zero above $y^+ \approx 700$ (Fig. 5). The positive and the negative peak values increase and the location where $\overline{vw} \approx 0$ in the profile is closer to the wall as the Vortex-core station is approached.

3. Transport-rate equations of the stresses

In this section first the stress transport-rate equations are introduced. Approximations made in determination of each of the terms in these equations are discussed next. The Reynolds stress transport equation with summation-subscript notation can be written as (Launder et al., 1975)

$$C_{ij} = \mathrm{PR}_{ij} + \Phi_{ij} + \mathrm{TD}_{ij} + \mathrm{PD}_{ij} + \mathrm{VD}_{ij} - \varepsilon_{ij}$$

where

$$C_{ij} = \frac{\partial \overline{u_i u_j}}{\partial t} + U_l \frac{\partial \overline{u_i u_j}}{\partial x_l} \quad \text{convection}$$

$$\mathrm{PR}_{ij} = -\left(\overline{u_i u_l} \frac{\partial U_j}{\partial x_l} + \overline{u_j u_l} \frac{\partial U_i}{\partial x_l} \right) \quad \text{production}$$

$$\Phi_{ij} = \overline{\frac{p}{\rho}\left(\frac{\partial u_i}{\partial x_j} + \frac{\partial u_j}{\partial x_i} \right)} \quad \text{pressure–strain}$$

$$\mathrm{TD}_{ij} = -\frac{\partial(\overline{u_i u_j u_l})}{\partial x_l} \quad \text{turbulent diffusion}$$

$$\mathrm{PD}_{ij} = -\frac{1}{\rho}\left(\frac{\partial(\overline{p u_j})}{\partial x_i} + \frac{\partial(\overline{p u_i})}{\partial x_j} \right) \quad \text{pressure-diffusion}$$

$$\mathrm{VD}_{ij} = +\nu \frac{\partial^2 \overline{u_i u_j}}{\partial x_l^2} \quad \text{viscous diffusion}$$

$$\varepsilon_{ij} = +2\nu \overline{\frac{\partial u_i}{\partial x_l} \frac{\partial u_j}{\partial x_l}} \quad \text{viscous dissipation}$$

The subscripts denote the axes. Repeated dummy indices in a multiplication denote summation. Note the minus sign in front of ε_{ij}.

In the individual stress transport equations the Φ_{ij}, PD_{ij}, ε_{ij} and Φ_{ij}, PD_{ij}, ε_{ij} terms can not be directly determined from the measured data. The terms involving the fluctuating pressure (Φ_{ij} and PD_{ij}) require instantaneous spatial flow field knowledge, since the flow history influences the fluctuating pressure due to the mathematical nature of the pressure fluctuations (Rotta, 1962). The Φ_{ij}, PD_{ij}, Φ_{ij}, PD_{ij}, ε_{ij} terms can not be measured currently, since the measurement of pressure fluctuations and viscous dissipation within a flow at high Reynolds numbers with reasonable accuracy very near a boundary is extremely difficult. On the other hand, the rest of the terms in the individual stress transport equations can be determined at a single point.

In the current study PD_{ij} and Φ_{ij}, PD_{ij}, ε_{ij} were estimated using existing models by Lumley (1978) and Hallbäck et al. (1990). The pressure-strain term, Φ_{ij}, PD_{ij}, ε_{ij} was determined by the difference of terms in the equation. All the other terms were determined by using either a Taylor series expansion or fitting a function to the data and calculating the derivatives of this function at that point of interest. The uncertainty in each term of the stress balance equations was obtained using the two values calculated for that individual term using the two different data sets acquired at the Separation station and using Chauvent's criterion to calculate the standard deviation. Uncertainties of 21–1 odds calculated as $\pm 2\sigma$ are tabulated in Table 2.

3.1. Model for ε_{ij}: Hallbäck et al. (1990) anisotropic dissipation rate model

The fact that the limiting value of the dissipation rate at the wall is not isotropic is noted by many researchers and different algebraic models have been proposed in the literature. Tagawa et al. (1991) argued that simple algebraic models could not capture the physics and developed a new closure scheme which is not algebraic. The analysis of ε_{ij} near the wall using the fluctuation continuity equation shows that (Launder and Reynolds, 1983; Lai and So, 1990; Mansour et al., 1988) the dissipation rate of $\overline{u^2}$ and $\overline{w^2}$ vary linearly with y near the wall, reaching a constant value at the wall. Also, the dissipation for $\overline{v^2}$ is zero at the wall and varies as y^2 near the wall. These wall limits require an anisotropic dissipation rate tensor for asymptotically correct modeling. In this study the effect of an anisotropic dissipation approximation on the stress transport budget is determined using the anisotropic dissipation rate algebraic model of Hallbäck et al. (1990). Other existing dissipation rate models such as the model of Lai and So (1990) and Speziale and Gatski (1997) were tested but were not used. They resulted in variations almost the same as the isotropic dissipation rate variation or the near wall dissipation rate values obtained below $y^+ = 50$ did not follow the existing direct-numerical simulation (DNS) solutions obtained such as by Abe et al. (2001). The model by Hallbäck et al. (1990) reportedly (Jakirlic and Hanjalic, 2002) poorly predicted the DNS solutions of Jakirlic

Table 2
21:1 odds + 2σ uncertainties of stress-transport terms for the six stresses

Transport of term	Convection	Production	Turbulent diffusion	Pressure-diffusion	Pressure-strain	Viscous diffusion	Dissipation rate
$\overline{u^2}$	0.0047	0.0086	0.0049	0.0009	0.011	0.00066	0.0073
	0.0068	0.015	0.0091	0.0014	0.019	0.00137	0.0108
$\overline{v^2}$	0.0021	0.0011	0.0011	0.0023	0.0076	0.00036	0.0073
	0.0011	0.0009	0.0009	0.0044	0.014	0.00074	0.0108
$\overline{w^2}$	0.0071	0.0029	0.0036	0.0008	0.0068	0.00022	0.0073
	0.0071	0.0049	0.0048	0.0008	0.0094	0.00045	0.0108
$\overline{uv}$	0.00132	0.0025	0.0016	0.0071	0.0089	0.00056	
	0.00144	0.0042	0.0022	0.0141	0.0162	0.00117	
$\overline{uw}$	0.0017	0.0047	0.0027	0.0005	0.0061	0.00067	
	0.0019	0.0077	0.0048	0.0005	0.0111	0.00014	
$\overline{vw}$	0.0014	0.0017	0.0011	0.0061	0.0077	0.00025	
	0.0010	0.0029	0.0010	0.0118	0.0140	0.00052	

Uncertainties are non-dimensionalized by u_τ^4. Numbers in the second row show the uncertainties below $y^+ = 100$.

(1997) and the Speziale and Gatski (1997) model was discussed as one of the most complete dissipation rate models by Gatski (2004). Even so, the Hallbäck et al. model was applied in the present work. This is because the near wall variations of the transport terms are predicted much closer in value to the DNS solutions than any other model, including the isotropic dissipation rate model. Fig. 6 shows the dissipation rate determined using the Hallbäck et al. (1990) model and using the Speziale and Gatski (1997) model, indicating that the latter model results in negative dissipation rates near the wall for the $\overline{v^2}$ stress and larger dissipation rates for $\overline{w^2}$ than that of $\overline{u^2}$ even in 2-D flows, due to the nature of the approximations made in the model development near wall.

Hallbäck et al. (1990) developed their explicit model relating the anisotropies of the dissipation rate tensor to the anisotropies of the Reynolds stress tensor using Lumley's invariant theory (1978). The general expression for the dissipation rate anisotropies given by the invariant theory was expanded using a power series of the Reynolds stress anisotropies. A series of mathematical and physical constraints were employed on this expansion to obtain the dissipation rate anisotropy tensor e_{ij}

$$e_{ij} = \left(\frac{\varepsilon_{ij}}{\varepsilon}\right) - \frac{2}{3}\delta_{ij}$$

and

$$e_{ij} = \left[1 + \alpha\left(\frac{1}{2}II - \frac{2}{3}\right)\right]a_{ij} - \alpha\left(a_{ik}a_{kj} - \frac{1}{3}II\delta_{ij}\right)$$

where

$$a_{ij} \equiv \left(\frac{\overline{u_i u_j}}{k}\right) - \frac{2}{3}\delta_{ij}, \quad k = \frac{1}{2}\overline{u_i u_i}, \quad II = a_{ik}a_{ki}, \quad \alpha = \frac{3}{4}$$

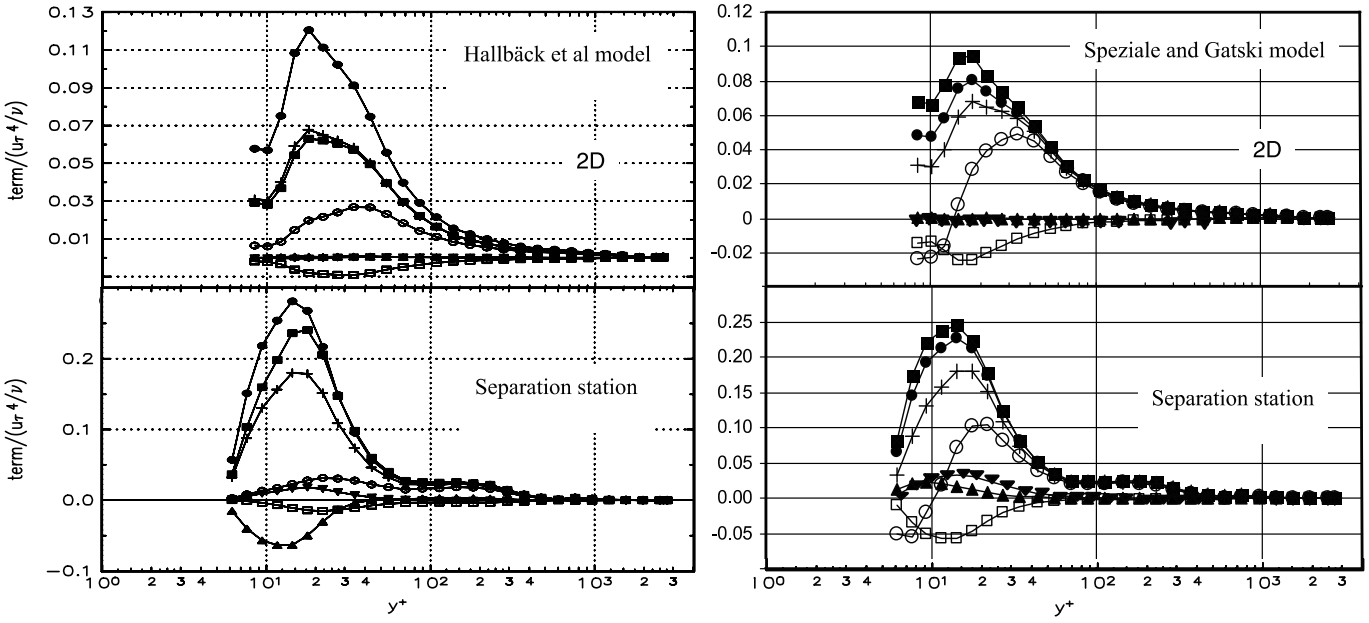

Fig. 6. Anisotropic dissipation rate distribution calculated using, left: Hallbäck et al. (1990) model right: Speziale and Gatski (1997) model at different stations, top: 2-D, bottom: Separation stations in tunnel coordinates. $\overline{u^2}$, ●; $\overline{v^2}$, ○; $\overline{w^2}$, ■; $\overline{uv}$, □; $\overline{uw}$, ▲; $\overline{vw}$, ▼; isotropic distribution, +.

The model was successfully tested against numerical simulations of homogeneous turbulence with success (Hallbäck et al., 1990).

The turbulent kinetic energy (TKE) dissipation rate, ε required in dissipation calculations for the stresses was estimated using the budget of the TKE transport equation. The TKE transport equation can be expressed as half of the sum of the transport equations for the normal stresses. (Convection of TKE $= \frac{1}{2}(C_{11} + C_{22} + C_{33})$). The pressure-strain term in the TKE transport equals zero since continuity for incompressible flows requires that ($\frac{\partial u_i}{\partial x_i} = 0$), leaving pressure-diffusion and viscous dissipation terms as the unknowns in the balance of the equation. This allows one to use an approximate model for one of the terms and extract the other term from the balance of the TKE transport. The pressure-diffusion term in the TKE transport-rate equation was determined using Lumley's approximation, which is discussed below.

3.2. Model for PD_{ij}: Lumley's (1978) pressure-diffusion model

The pressure-diffusion term for a homogenous flow was modeled by Lumley (1978) using a Gaussian model. Using a moment generating function to produce an equivalent scalar joint velocity density function and using Fourier transforms for homogeneous stochastic fields (Lumley, 1970), Lumley obtained the following equation

$$\frac{1}{\rho}\overline{pu_k} = -\frac{1}{5}\overline{(u_k(u^2 + v^2 + w^2)}$$

Although the effect of the pressure-diffusion term was assumed to be small in previous studies (Schwarz and Bradshaw, 1994) above $y^+ \approx 150$, the pressure-diffusion term is not necessarily small at lower y^+ as shown by Launder and Tselepidakis (1990) and Sumitani and Kasagi (1995). Launder and Tselepidakis showed that pressure diffusion has substantial importance in shaping the sublayer turbulence structure, while DNS studies of Sumitani, and Kasagi show that the pressure-diffusion terms for the normal and shear stresses are as large as the pressure-strain term below $y^+ \approx 10$. In addition the pressure-diffusion term for the TKE balance is practically zero, which is also approximately true for the pressure-diffusion terms estimated for the TKE equation using Lumley's approximation. In this study the pressure-diffusion term was not neglected to avoid large errors that would result in the individual pressure-strain terms extracted from the data, especially near the wall. The error introduced by using Lumley's approximation is believed to be smaller than neglecting it. If the pressure-diffusion term is neglected, the pressure-strain term extracted also includes the pressure-diffusion term in it. Current study also indicates that the pressure-diffusion terms are small away from the wall above $y^+ \approx 100$.

The constant multiplier (1/5) used in Lumley's approach was questioned by several researchers. Although Launder and Tselepidakis (1990) used the same form of Lumley's equation, the constant multiplier used was 0.15, which was not derived through a rigorous analysis. Large-eddy simulations of Shao et al. (1990), of a shearless turbulent mixing layer flow shows that the constant (1/5) may be an overestimation. The constant multiplier was also discussed in Shih et al. (1987), but a new number was not proposed. In the present paper the constant multiplier is the same as proposed by Lumley, as this is the best estimate to date.

4. Results and discussion

In this section the role and relative importance of each term in the transport-rate equations both in 2-D and 3-D flows are separately examined to aid future model development. Experimentally determined TKE and the stress budgets were compared to the 2-D turbulent channel flow DNS solutions by Mansour et al. (1988) and Moser et al. (1999) and 3-D DNS solutions of Moin et al. (1990) on a 3DTBL generated with a sudden pressure gradient on a 2-D fully developed plane channel flow using DNS. The results in general show a good agreement between the budgets and the DNS solutions, although the DNS solutions show terms closer to zero at $y^+ \approx 150$ where in the present data the values are different than zero up to $y^+ \approx 1500$.

4.1. Some observations on the transport-rate equations using current data

In the current 2-D flow, while the V component of the velocity is two orders of magnitude smaller than the U component, the W component is zero. The main strain rate is due to the U velocity component perpendicular to the wall and the $\overline{uw}$ and $\overline{vw}$ shear stresses are zero due to no cross flow. The largest production term, $-\overline{uv}\frac{\partial U}{\partial y}$ of $\overline{u^2}$ stress, is much larger than the $\overline{v^2}$ production term $-\overline{v^2}\frac{\partial V}{\partial y} - \overline{uv}\frac{\partial V}{\partial y}$ and the largest $\overline{w^2}$ production term $-\overline{v^2}\frac{\partial V}{\partial y} - \overline{uv}\frac{\partial V}{\partial y}$ is practically zero since $\overline{uw}$, $\overline{vw}$ and $\partial W/\partial y$ are zero. The $\overline{v^2}$ production rate is approximately zero not only because $\frac{\partial V}{\partial y}$ is small but because $\frac{\overline{v^2}}{-\overline{uv}} \approx 1$ in a 2-D boundary layer. Therefore the TKE production in a 2-D flow is mainly due to the $\overline{u^2}$ production. The largest $\overline{uv}$ production term component is $-\overline{v^2}\frac{\partial U}{\partial y}$.

In general, the trace of the pressure-strain tensor Φ_{ij} is zero due to the incompressible continuity equation ($\frac{\partial u_i}{\partial x_i} = 0$), indicating that the sum of the pressure-strain terms for the normal stress transport equations and, therefore, the pressure-strain term for the TKE transport equation is zero.

In a 3-D flow the existence of a W mean velocity gradient is the main cause of the production of $\overline{w^2}$ normal stress and $\overline{uw}$ and $\overline{vw}$ stresses, where the main production terms for these stresses are $(-\overline{vw}\frac{\partial W}{\partial y})$, $(-\overline{uv}\frac{\partial W}{\partial y} - \overline{vw}\frac{\partial U}{\partial y})$, and $(-\overline{v^2}\frac{\partial W}{\partial y} - \overline{vw}\frac{\partial V}{\partial y})$, respectively. As these terms indicate, the production of the $\overline{vw}$ stress together with the W mean veloc-

ity gradient results in the production of the $\overline{w^2}$ and increases the production of the $\overline{uw}$ stress; this indicates the importance of the $\overline{vw}$ stress in 3-D flows. Since the trace of the pressure-strain term is zero also for the 3-D flows, the energy extracted by the pressure-strain terms in the budgets of the normal stresses are distributed among the normal stresses.

4.2. Turbulent kinetic energy transport-rate budgets

TKE budgets (Fig. 7) show that at every station the dissipation rate and the production terms follow each other closely above $y^+ \approx 40$, and also above $y^+ \approx 100$ and that these are the major terms with other terms being closer to zero. Both the production and the dissipation profiles peak at around $y^+ \approx 15$–20. Compared to the production and dissipation terms, the pressure-diffusion is much smaller throughout the layers, which shows that the dissipation term calculated from the TKE budget balance using Lumley's approach for the pressure-diffusion term does not have a substantial effect on the overall TKE budget. The pressure-diffusion terms have opposite signs to viscous diffusion and turbulent diffusion near the wall below

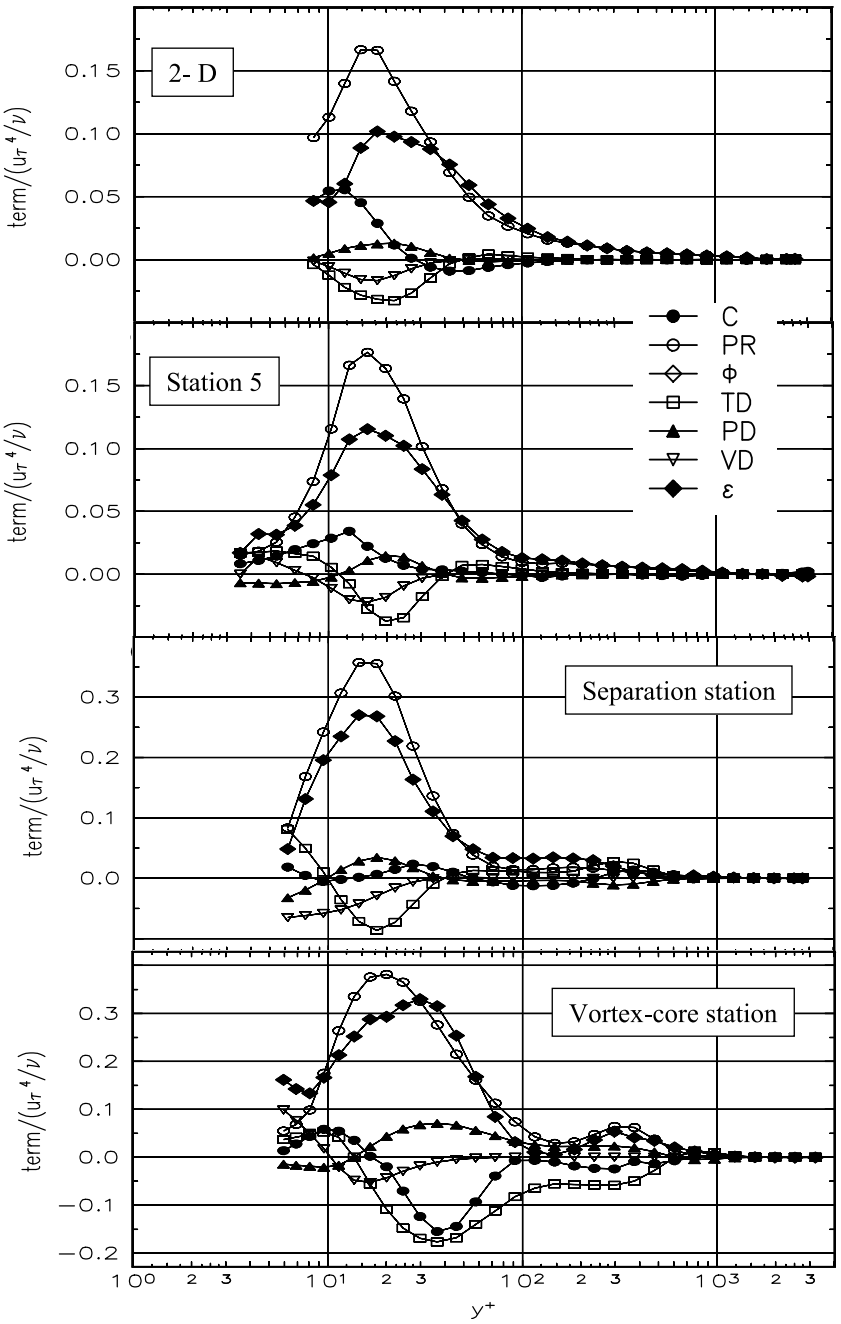

Fig. 7. Turbulent kinetic energy transport budget at different stations, top to bottom: (a) 2-D, (b) Station 5, (c) Separation, (d) Vortex-core stations in tunnel coordinates. Symbols denote, ●, convection (C); ○, production (PR); ◇, pressure-strain (φ); □, turbulent diffusion (TD); ▲, pressure-diffusion (PD); ▽, viscous diffusion (VD); ♦, dissipation (ϵ).

$y^+ \approx 35$, and each of these terms changes sign around $y^+ \approx 10$ at every station.

At the Separation station the TKE budget balance shows that, except the convection terms all the term values are more than twice those at Station 5 (Fig. 7). At the Vortex-core while the production and dissipation values are close to the values at the Separation station, the convection, turbulent diffusion, pressure-diffusion terms are much increased. All the terms except the viscous diffusion are important throughout the layers, and the effects of the terms are not confined to $y^+ < 100$.

Term-by-term comparison of the variations are similar to the variations observed by Compton and Eaton (1997) for an initially 2DTBL becoming a 3DTBL due to negotiating a 308 corner while their free-stream velocity is about 12.5 m/s, $Re_\theta = 4000$ for the approach flow, and the u_τ values are about less than half the values observed in the current study for the 2-D case. They indicate that the

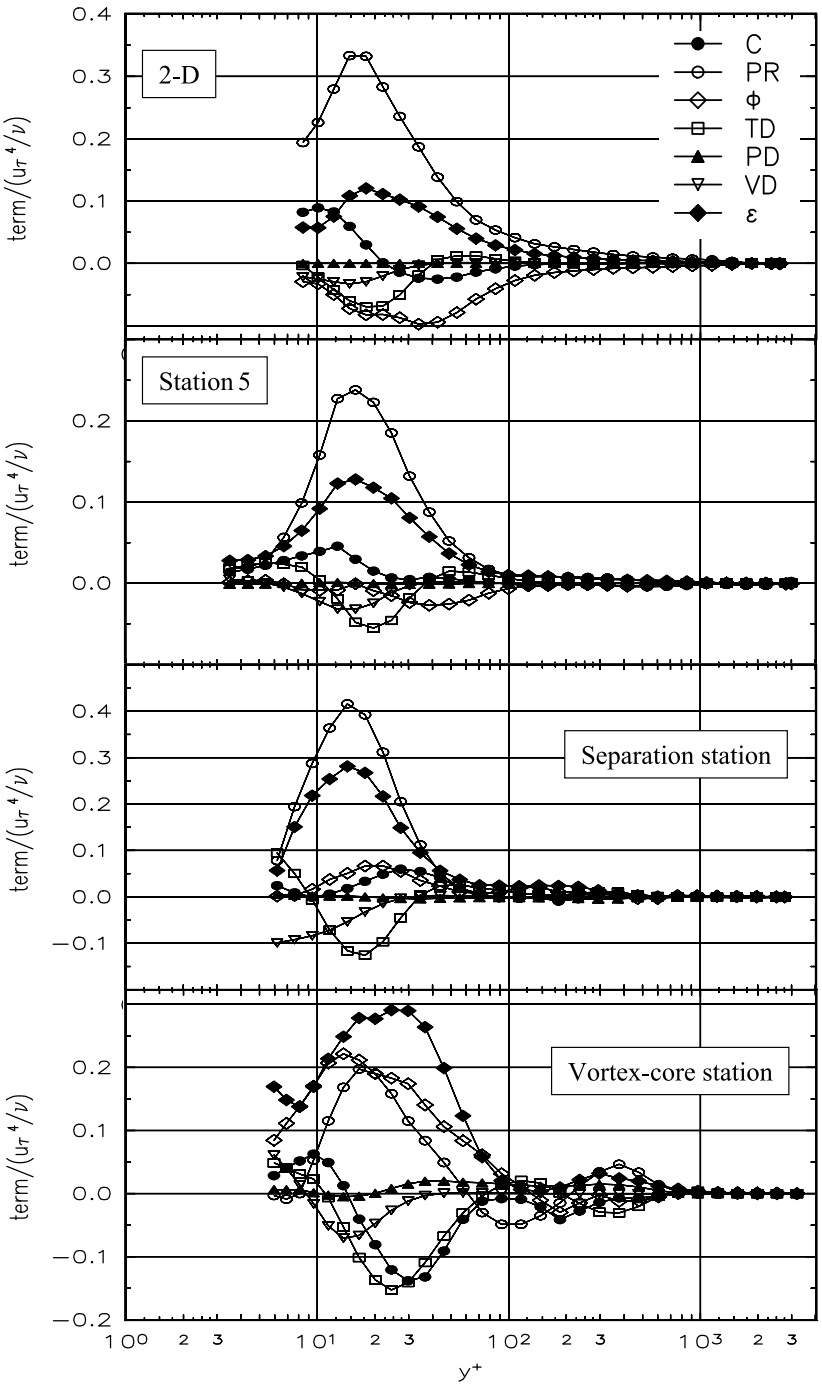

Fig. 8. $\overline{u^2}$ normal stress transport budget at different stations top to bottom: (a) 2-D, (b) Station 5, (c) Separation, (d) Vortex-core stations in tunnel coordinates. Legend is same as Fig. 7.

production and the dissipation rates for the 2-D and the 3-D flows are about the same (Fig. 16 of Compton and Eaton, 1997) with slight increase in the terms for the 3-D case, similar to the observations made in the current study (Fig. 7 for the 2-D and Station 5 budgets). Bruns et al. (1999) using their data obtained in an S shaped duct indicate that (their Fig. 31) the production and the dissipation are practically equal to each other above $y^+ = 40$, similar to the observations made here. The DNS calculations made by Moin et al. (1990) of a planar channel flow with impulsively started transverse pressure gradient indicate that near the wall at $y^+ = 10$ the dissipation term is about 0.5 times the production term for the 2-D flow case, although the dissipation rate becomes 1.5 times the production rate with increased three-dimensionality. Similar results are obtained by DNS solutions of Coleman et al. (2000) for an initially fully developed and two-dimensional channel flow subjected to mean strains thus emulating the effect

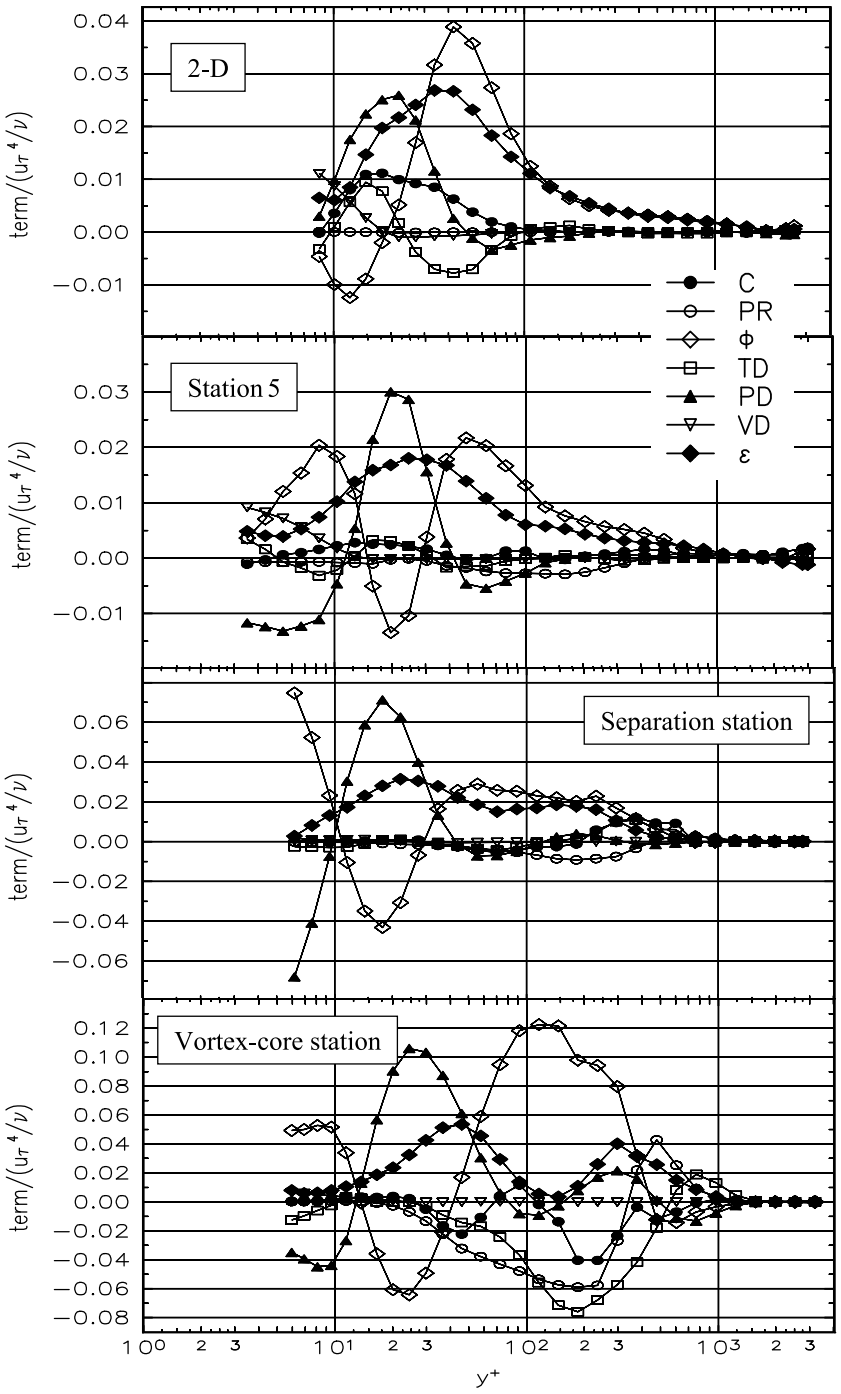

Fig. 9. $\overline{v^2}$ normal stress transport budget at different stations top to bottom: (a) 2-D, (b) Station 5, (c) Separation, (d) Vortex-core stations in tunnel coordinates. Legend is same as Fig. 7.

of rapid changes of streamwise and spanwise pressure gradients in three-dimensional boundary layers (their Section 3.2).The observations made here indicate that the TKE budget terms as calculated are similar to the variations observed in DNS calculations for the 2-D case and similar to the other experimental data for 3-D flows; the decrease in production and increase in dissipation observed by DNS in 3-D flows is not observed in the current study.

4.3. Stress transport-rate equation budgets

The transport-rate terms for the Reynolds stresses are plotted in Figs. 8–13 for the $\overline{u^2}, \overline{v^2}, \overline{w^2}, \overline{uv}, \overline{uw}$, and the $\overline{vw}$ stresses, respectively. At Station 5, Separation and Vortex-core stations the distributions of the transport budget terms decrease progressively more steeply approaching zero values compared to the 2-D flow station at lower y^+ locations for the $\overline{u^2}, \overline{w^2}$, and $\overline{uv}$ stresses. This may be due

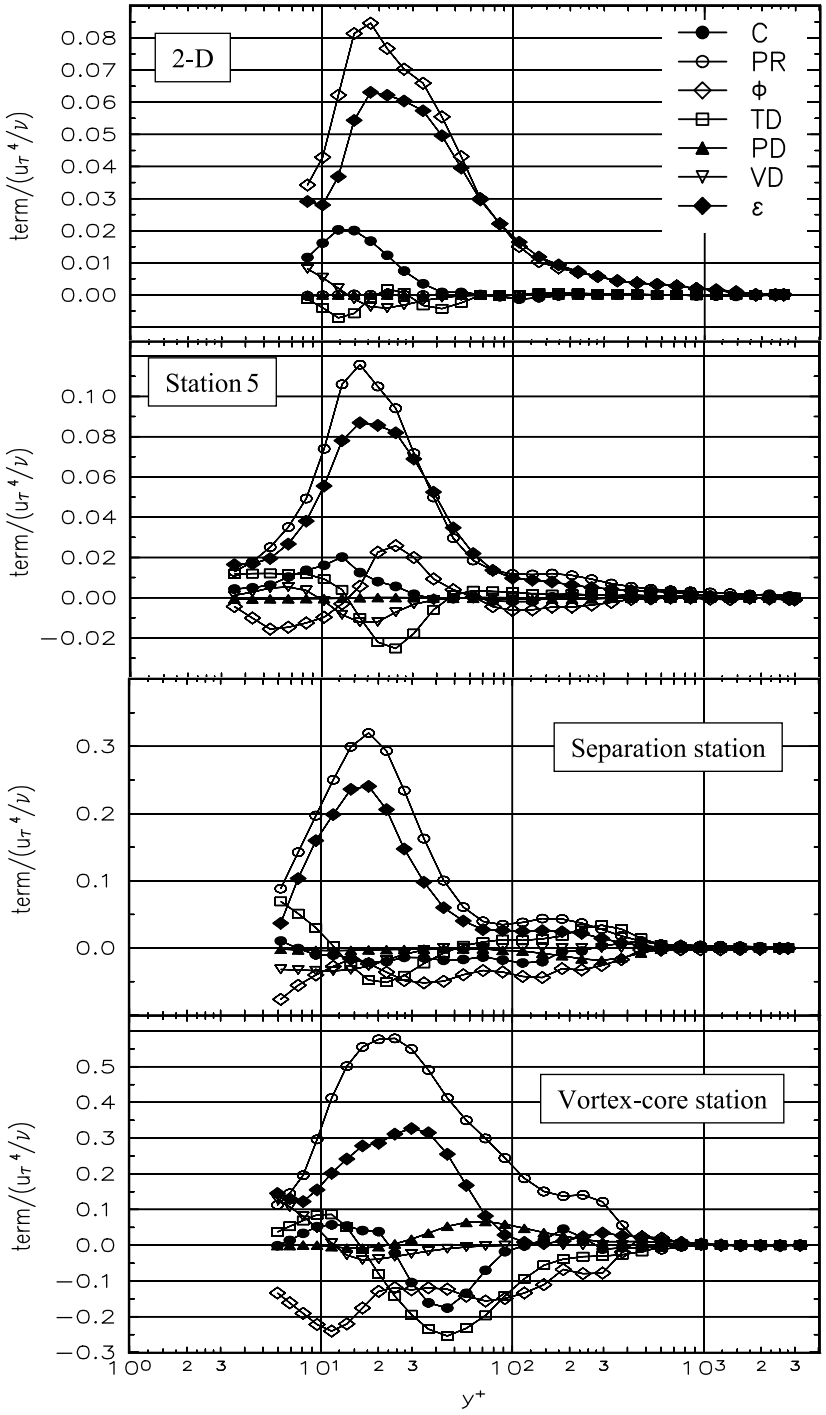

Fig. 10. $\overline{v^2}$ normal stress transport budget at different stations, top to bottom: (a) 2-D, (b) Station 5, (c) Separation, (d) Vortex-core stations in tunnel coordinates. Legend is same as Fig. 7.

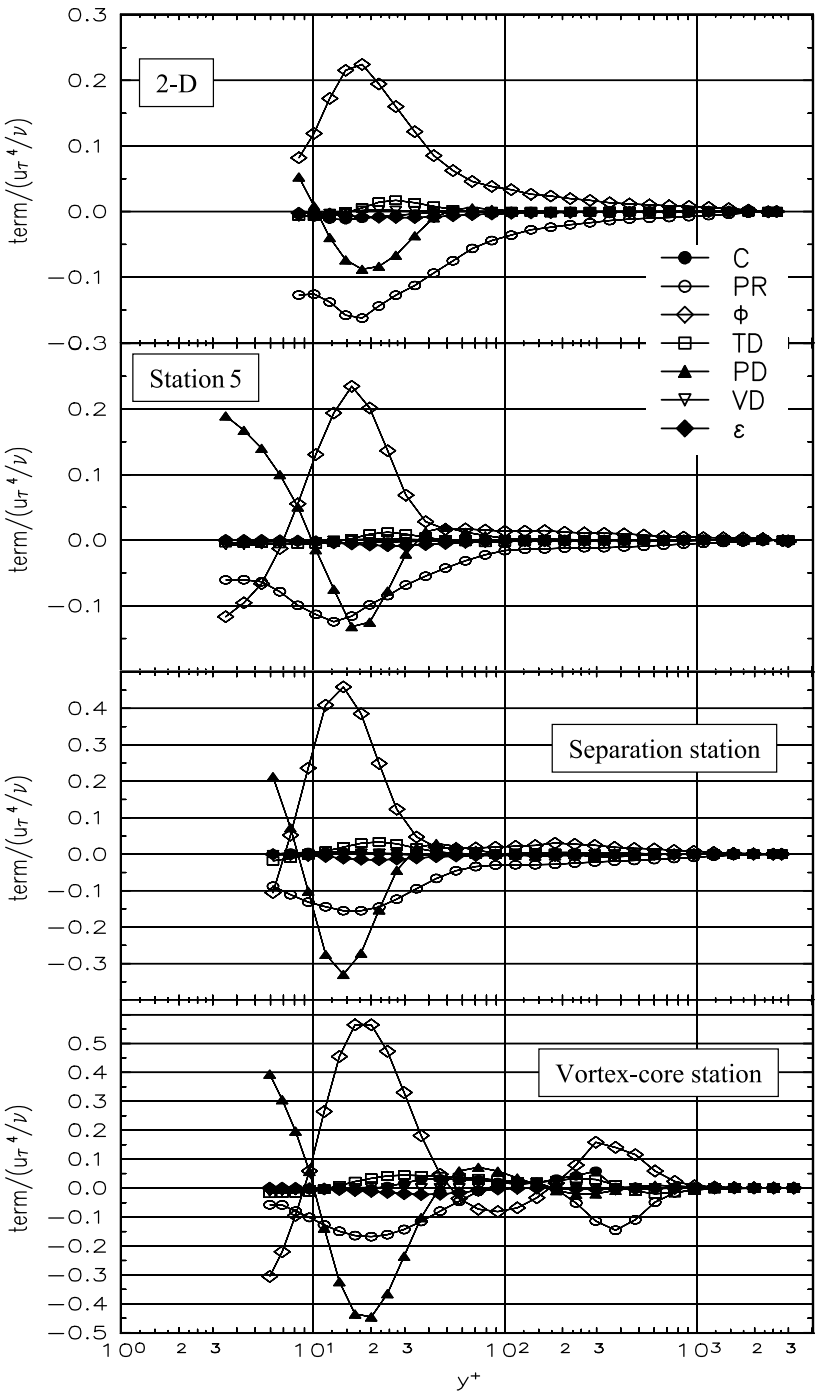

Fig. 11. $\overline{uv}$ shear stress transport budget at different stations, top to bottom: (a) 2-D, (b) Station 5, (c) Separation, (d) Vortex-core stations in tunnel coordinates. Legend is same as Fig. 7.

to the three-dimensionality of the flow stabilizing the near wall boundary layer as observed by Flack (1997) in the study of a 30.8 bend flow showing a decreased number of vortical ejection events in 3DTBL regions. At the Vortex-core station observations made here are accompanied with the effects of the outer region vortex which produces substantial terms.

The production of the $\overline{u^2}$ and $\overline{w^2}$ stresses are comparable to each other in 3-D flows with their peak at $y^+ \approx 20$. While the production of $\overline{w^2}$ increase with increased three-dimensionality and is positive throughout the layers, the $\overline{u^2}$ production does not show a trend. The $\overline{v^2}$ production becomes less than zero above $y^+ \approx 30$ (Fig. 9), while the $\overline{uv}$ (Fig. 11), and $\overline{uw}$ (Fig. 12) production terms are less than zero throughout the layers with their peak at $y^+ \approx 20$ and $y^+ \approx 15$, respectively. The $\overline{vw}$ (Fig. 13) production peaks at $y^+ \approx 20$ with a positive sign, however it becomes negative over $y^+ \approx 100$, presumably responding to the change

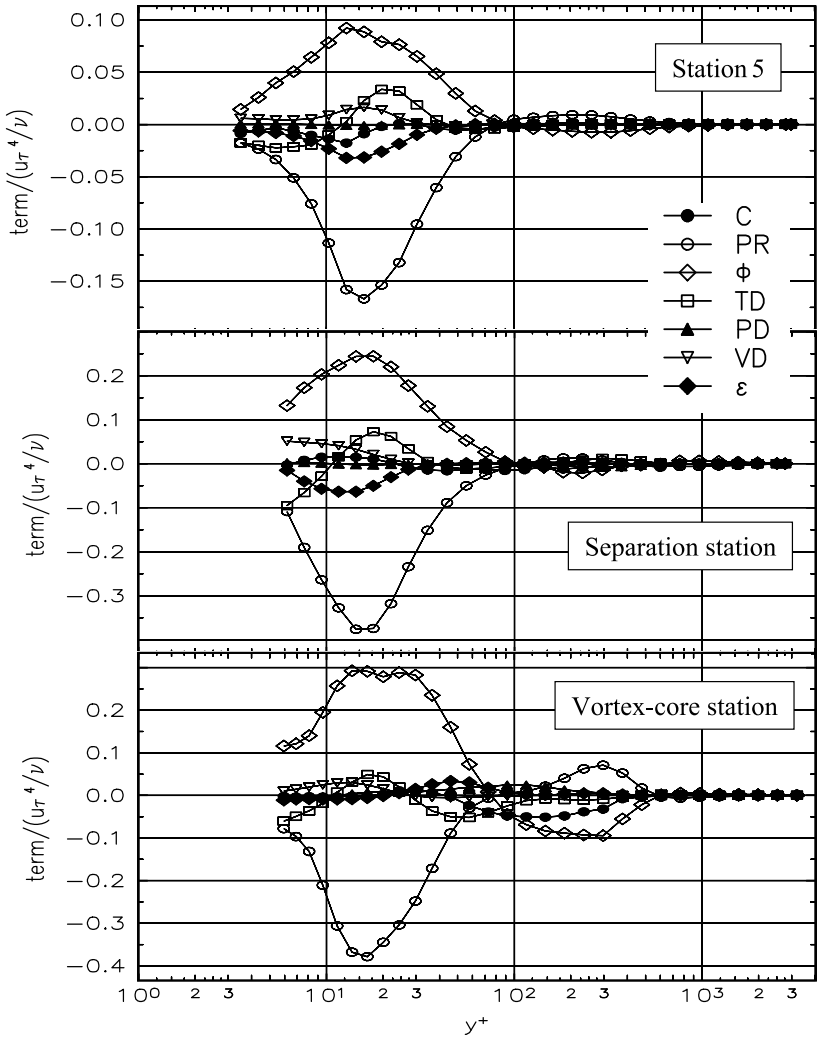

Fig. 12. $\overline{uw}$ shear stress transport budget at different stations, top to bottom: (a) Station 5, (b) Separation, (c) Vortex-core stations in tunnel coordinates. Legend is same as Fig. 7.

in sign of the W mean velocity gradient, $-\overline{vw}\frac{\partial W}{\partial y}$. For $\overline{v^2}$, the mainly pressure-strain term is the term that aids in energizing $\overline{v^2}$. While the magnitude of the $\overline{uv}$ production rate is about the same for the 2-D and the 3-D flows, the production rate increases for the $\overline{uw}$ and $\overline{vw}$ stresses at 3-D flow stations.

The dissipation rate for the $\overline{u^2}$ and the $\overline{w^2}$ stresses increase with increased three-dimensionality, while the $\overline{v^2}$ stress dissipation rate first decreases at Station 5 but increases at the Separation and the Vortex stations. Although the dissipation rates for the shear stresses are close to zero, they are not zero due to the anisotropic nature of the dissipation rate equation used (Hallbäck et al., 1990). The dissipation rate of $\overline{uv}$ and $\overline{vw}$ stresses is about half of the $\overline{v^2}$ terms. For 3-D flow stations the dissipation rate distributions are approximately isotropic above y^+.100. However for 2-D flow it becomes isotropic above y^+.350. While the $\overline{v^2}$ and $\overline{uv}$ dissipation rates are zero, the $\overline{u^2}$ and the $\overline{w^2}$ dissipation rates are different than zero at the wall for 2-D flows, with their magnitudes being equal to the viscous diffusion at the wall (Bernard and Wallace, 2002, pp. 126–130).

The pressure-diffusion term has a large affect on shaping the transport rate budgets near the wall. The relative magnitude of the pressure-diffusion and pressure-strain terms with respect to that of the production term increases with increased three-dimensionality for $\overline{v^2}, \overline{uv}$, and $\overline{vw}$, while the pressure-diffusion and pressure-strain term trends tend to be opposed to each other indicating that the effect of the terms is mostly to cancel one another. The pressure-diffusion terms are practically zero for all the other stresses at every station. The major pressure-diffusion terms for the $\overline{v^2}, \overline{uv}$, and $\overline{vw}$, stresses are $\frac{\partial(\overline{pu})}{\partial y}, \frac{\partial(\overline{pv})}{\partial y}, \frac{\partial(\overline{pw})}{\partial y}$, respectively. Increased values of non-dimensional pressure-diffusion indicate that the differences between the correlation values in the layers are increasing with increasing three-dimensionality of the flow.

The pressure-strain term shows the correlation between the pressure fluctuations and the fluctuating velocity gradients and is important in shaping the near wall structure at

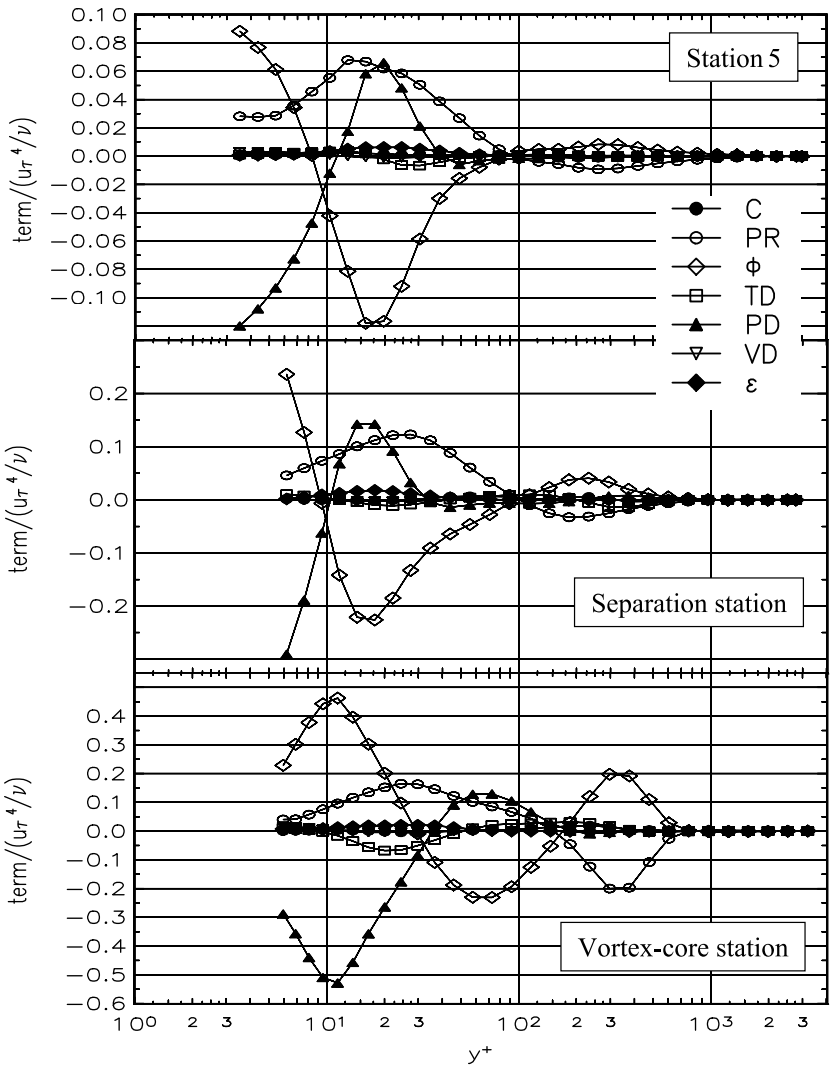

Fig. 13. $\overline{vw}$ shear stress transport budget at different stations, top to bottom: (a) Station 5, (b) Separation, (c) Vortex-core stations in tunnel coordinates. Legend is same as Fig. 7.

every station for every stress. At the 2-D station, while the pressure-strain term is negative throughout the layer for the $\overline{u^2}$ components, it is positive for the $\overline{w^2}$ component and changes sign to become positive around $y^+ = 20$ for the $\overline{v^2}$ component. With increasing three-dimensionality the pressure-strain value, Φ_{11}, (for the $\overline{u^2}$ stress) becomes positive indicating that the positive pressure fluctuations occur more together with the positive $\partial u/\partial x$ gradients; Φ_{33}, pressure-strain value (for the $\overline{w^2}$ stress) becomes negative indicating that the opposite signed pressure and $\partial w/\partial z$ fluctuating velocity gradients occur more together in 3-D flows. Since the sum of the pressure-strain terms in the TKE transport equation is zero, negative pressure-strain term for a normal stress must be compensated by the sum of the pressure-strain terms for the other normal stresses. At the Separation and the Vortex-core stations the sign of the $\overline{u^2}$ pressure-strain changes to positive, with the largest magnitude occurring at the Vortex-core station. At these stations the $\overline{v^2}$ strain rate becomes negative between $y^+ = 10$ and 30 and the $\overline{w^2}$ pressure-strain is negative throughout the layers resulting in positive $\overline{u^2}$ pressure-strain term; this energizes $\overline{u^2}$ by extracting energy from other normal stresses. Positive values below $y^+ = 10$ and above $y^+ = 30$ in the $\overline{v^2}$ transport equations indicate the fact that $\overline{w^2}$ also energizes $\overline{v^2}$ at the 3-D stations. For the shear stress values the pressure-strain values are increased with increased three-dimensionality; this indicates that the fluctuating velocity component gradients along the off-axis directions (such as u gradient in the y or z directions) are becoming better correlated with the pressure fluctuations. The pressure-strain term peak value magnitude increases with increased three-dimensionality for all the shear stresses.

Turbulent diffusion shows the negative of the spatial variation of the work rate done by the stresses in the direction of the flow. The data indicates that the turbulent diffusion term is different than zero for all the stresses at every station especially near the wall, with both positive and negative values observed. Turbulent diffusion effects are observed to be significant below $y^+ \approx 40$, for all the

stations except the Vortex-core station, where the effects are observed throughout the layers for the normal stresses. Turbulent diffusion is positive below $y^+ \approx 10$ and negative up to $y^+ \approx 40$ for $\overline{u^2}, \overline{w^2}, \overline{vw}$, while the signs are the opposite for the $\overline{uv}$ and $\overline{uw}$ stresses at the 2-D, Station 5 and the Separation stations. The peak value magnitude of the turbulent diffusion increases with increased three-dimensionality, except for the $\overline{v^2}$ stress.

The viscous diffusion for a stress is the sum of the second derivatives of a stress in the x, y, and z directions multiplied by the kinematic viscosity. Viscous diffusion terms are observed to be significant below $y^+ \approx 40$ for $\overline{u^2}, \overline{w^2}$ and the $\overline{uw}$ stresses, but approximately zero for the other stress transport equations at all stations.

The magnitude of the convection term is observed to decrease at Station 5 and Separation stations compared to the 2-D values for $\overline{u^2}, \overline{v^2}, \overline{w^2}$ stresses, while the peak location shifts away from the wall. For the Vortex station, near wall positive peak is accompanied by a negative peak away from the wall for these normal stresses. For the $\overline{uv}, \overline{uw}$, and $\overline{vw}$ stresses the values are fairly close to zero. If the convection term is zero it denotes that the variation of the quantity following a mean flow streamline is zero. The convection term must be kept, as small as it may be, for variation of the stresses.

5. Conclusions

Experimental velocity data obtained in a wing/body junction flow at selected stations and in a 2DTBL are used to study the transport-rate budgets of the normal and shear stresses. While the pressure-diffusion term was approximated by Lumley, 1978('s model), the dissipation rate was approximated by Hallbäck et al. model (1990) and the pressure-strain term was determined from the balance of the transport-rate equations. Other terms in the transport equations were calculated using the experimental data. Some conclusions that can be made from the current study are as follows:

(1) The production of $\overline{w^2}$ increases with increased three-dimensionality; the $\overline{u^2}$ production does not show a trend. The production term that is about zero for $\overline{v^2}$ in the 2-D flow becomes negative above $y^+ \approx 30$ with increased three-dimensionality. While the magnitude of the $\overline{uv}$ production rate is about the same for the 2-D and the 3-D flows, the production rate increases for the $\overline{uw}$, and $\overline{vw}$ stresses with increased three-dimensionality.

(2) While the dissipation rates for $\overline{u^2}$ and $\overline{w^2}$ increase, the $\overline{v^2}$ dissipation rate decreases with increased three-dimensionality. The dissipation rate distributions are approximately isotropic above $y^+ \approx 100$ for the 3-D flow stations, and above $y^+ \approx 350$ for the 2-D flow. The dissipation rates for the shear stresses are close to zero.

(3) The pressure-diffusion term largely affects the transport-rate budget of the $\overline{v^2}$ normal stress and the $\overline{uv}$ and $\overline{vw}$ shear stresses. The magnitude of the term increases with increased three-dimensionality. The effect of the term is negligible for the transport-rate budget of the TKE and other stresses.

(4) Although the $\overline{u^2}$ pressure-strain term is negative in the 2DTBL, its magnitude reduces with increased three-dimensionality and it is positive at the Separation and Vortex-core stations. On the other hand the positive $\overline{w^2}$ pressure-strain term observed in the 2DTBL reduces at 3-D stations and its sign becomes negative at the Separation and Vortex-core stations. While the energy extracted by the $\overline{u^2}$ pressure-strain term energizes $\overline{w^2}$ and $\overline{v^2}$ for most of the layer in the 2DTBL, at the Separation and the Vortex-core stations the $\overline{w^2}$ pressure-strain term energizes $\overline{u^2}$ and $\overline{v^2}$ through most of the layers. The pressure-strain term magnitude for the $\overline{uv}, \overline{uw}, \overline{vw}$ stresses increases with increased three-dimensionality.

References

Abe, H., Kawamura, H., Matsuo, Y., 2001. Direct numerical simulation of a fully developed turbulent channel flow with respect to the reynolds number dependence. J. Fluids Eng., Trans. ASME 123 (June).

Ailinger, K., 1990. Measurements of surface shear stresses under a three-dimensional turbulent boundary layer using oil-film interferometry, MS thesis, Report VPI-AOE-173, Virginia Tech, Aerospace and Ocean Engineering Department, Blacksburg, VA 24061.

Apsley, D.D., Leschziner, M.A., 2001. Investigation of advanced turbulence models for the flow in a generic wing–body junction flow. Turbulence and Combustion 67, 25–55.

Bernard, P.S., Wallace, J.M., 2002. Turbulent Flow, Analysis, Measurement and Prediction. John Wiley and Sons.

Bonnin, J.C., Buchel, T., Rodi, W., 1996. ERCOFTAC Workshop on Data bases and Testing of Calculation Methods for Turbulent Flows, ERCOFTAC Bulletin 28, March 1996.

Bruns, J.M., Fernholz, H.H., Monkewitz, P.A., 1999. An experimental investigation of a three-dimensional turbulent boundary layer in an 'S'-shaped duct. J. Fluid Mech. 393, 175–213.

Compton, D.A., Eaton, J.K., 1997. Near-wall measurements in a three-dimensional turbulent boundary layer. J. Fluid Mech. 350, 189–208.

Coleman, G.N., Kim, J., Spalart, P., 2000. A numerical study of strained three-dimensional wall-bounded turbulence. J. Fluid Mech. 416, 75–116.

Coles, D., 1956. The law-of-the-wake in the turbulent boundary layer. J. Fluid Mech. 1 (Part 2), 191–226.

Deng, G., Visonneau, M., 1999. Computation of a wing–body junction flow with a new Reynolds-stress transport model. In: Proc. 22nd Symp Naval Hydor.. National Academies Press, pp. 691–707.

Devenport, W.J., Simpson, R.L., 1990. A time-dependent and time-averaged turbulence structure near the nose of a wing–body junction. J. Fluid Mech. 210, 23–55.

Devenport, W.J., Simpson, R.L., 1992. Flow past a wing–body junction – experimental evaluation of turbulence models. AIAA J. 30 (4), 873–882.

Flack, K.A., 1997. Near-wall structure of three-dimensional turbulent boundary layers. Exp. Fluids 23, 335–340.

Fleming, J., Simpson, R.L., Devenport, W.J., 1993. An experimental study of a turbulent wing–body junction and wake flow. Exp. Fluids 14, 366–378.

Fleming, J., Simpson, R.L., Shinpaugh, K.A., 1995. Further investigation of the near wall flow structure of a low Reynolds number 3-D turbulent boundary layer. AIAA paper AIAA-95-0788, 33rd Aerospace sciences meeting and exhibit, January 9–12, Reno, NV.

Gatski, T.B., 2004. Constitutive equations for turbulent flows. Theoret. Comput. Fluid Dyn. 18, 345–369.

Ha, S.M., Simpson, R.L., 1993. An experimental study of coherent structures in a three dimensional turbulent boundary layer, Report# VPI-AOE-205, Virginia Tech, Aerospace and Ocean Engineering Department, Blacksburg, VA 24061.

Hallbäck, M., Groth, J., Johansson, A.V., 1990. An algebraic model for nonisotropic turbulent dissipation rate in Reynolds stress closure, October. Phys. Fluids A 2 (10), 1859–1866.

Itoh, M., Kobayashi, M., 2000. Turbulent structure in the three-dimensional boundary layer on a swept wing. Int. J. Heat Fluid Flow 21, 271–277.

Jakirlic, S. 1997. Reynolds-Spannungsmodellierung komplexer turbulenter Strömungen. Ph.D. Thesis, Erlangen-Nuremberg University.

Jakirlic, S., Hanjalic, K., 2002. A new approach to modelling near-wallturbulence energy and stress dissipation. J. Fluid Mech. 459, 139–166.

Kim, S., Walker, D.A., Simpson, R.L., 1991. Observation and measurement of flow structures in the stagnation region of a wing–body junction, Report# VPI-E-91-20, Virginia Tech, Engineering Science and Mechanics Dept., Blacksburg, VA 24061.

Lai, Y.G., So, R.M.C., 1990. On near-wall turbulent flow modeling. J. Fluid Mech. 221, 641–673.

Launder, B.E., Tselepidakis, D.P., 1990 (Contribution to the second-moment modeling of sublayer turbulent transport). In: Kline, S.J., Afgan, N.H. (Eds.), 1988 Zoran Zaric Memorial Conference. Near-wall Turbulence, 818–833.

Launder, B.E., Reynolds, W.C., 1983. Asymptotic near-wall dissipation rates in a turbulent flow. Phys. Fluids 26 (5), 1157–1158.

Launder, B.E., Reece, G.J., Rodi, W., 1975. Progress in the development of a Reynolds-stress turbulence closure. J. Fluid Mech. 68 (part 3), 537–566.

Lewis, D.J., Simpson, R.L., Diller, T., 1994. Time resolved surface heat flux measurements in the wing/body junction vortex. AIAA J., Thermophys. Heat Transfer 8, 656–663.

Lumley, J.L., 1970. Stochastic Tools in Turbulence. Academic Press, New York.

Lumley, J.L., 1978. Computation modeling of turbulent flows. Adv. Appl. Mech. 18, 124–176.

Mansour, N.N., Kim, J., Moin, P., 1988. Reynolds-stress and dissipation-rate budgets in a turbulent channel flow. J. Fluid Mech. 194, 15–44.

Moin, P., Shih, T.H., Driver, D., Mansour, N.N., 1990. Direct numerical simulation of a three-dimensional turbulent boundary layer. Phys. Fluids A 2 (10), 1846–1853.

Moser, R.D., Kim, J., Mansour, N.N., 1999. DNS of turbulent channel flow up to $R_\tau = 590$. Phys. Fluids 11, 943–945.

Ölçmen, M.S., 1990. An experimental study of a three-dimensional pressure-driven turbulent boundary layer, Ph.D. Dissertation, Virginia Tech, Aerospace and Ocean Engineering Department, Blacksburg, VA 24061.

Ölçmen, M.S., Simpson, R.L., 1994. Influences of wing shapes on the surface pressure fluctuations of a wing–body junction. AIAA J. 32 (1), 6–15.

Ölçmen, M.S., Simpson, R.L., 1995a. An experimental study of a three-dimensional pressure-driven turbulent boundary layer. J. Fluid Mech. 290, 225–262.

Ölçmen, M.S., Simpson, R.L., 1995b. A five-velocity-component laser-Doppler velocimeter for measurements of a three-dimensional turbulent boundary layer. Meas. Sci. Technol. 6, 702–716.

Ölçmen, M.S., Simpson, R.L., 1996a. Experimental evaluation of pressure-strain models in complex 3-D turbulent flow near a wing/body junction, Report# VPI-AOE-228, Virginia Tech, Aerospace and Ocean Engineering Department, Blacksburg, VA 24061; DTIC-ADA307116. <http://stinet.dtic.mil/cgi-bin/GetTRDoc?AD=A307116&Location=U2&doc=GetTRDoc.pdf>.

Ölçmen, M.S., Simpson, R.L., 1996b. Experimental transport-rate budgets in complex 3-D turbulent flow near a wing/body junction, AIAA-1996-2035, 27th AIAA Fluid Dynamics Conference, June 17–20, New Orleans, LA.

Ölçmen, M.S., Simpson, R.L., 1996c. Theoretical and experimental pressure-strain comparison in a pressure-driven three-dimensional turbulent boundary layer, AIAA-1996-2141, 1st AIAA Theoretical Fluid Mechanics Meeting, June 17–20, New Orleans, LA.

Ölçmen, M.S., Simpson, R.L., 1996d. Some structural features of a turbulent wing–body junction vortical flow, Report# VPI-AOE-238, Virginia Tech, Aerospace and Ocean Engineering Department, Blacksburg, VA 24061; DTIC- ADA321557. <http://stinet.dtic.mil/cgi-bin/GetTRDoc?AD=A321557&Location=U2&doc=GetTRDoc.pdf>.

Ölçmen, M.S., Simpson, R.L., 1996e. Higher order turbulence results for a three-dimensional pressure-driven turbulent boundary layer, Report# VPI-AOE-237, Virginia Tech, Aerospace and Ocean Engineering Department, Blacksburg, VA 24061; DTIC- ADA321516. <http://stinet.dtic.mil/cgi-bin/GetTRDoc?AD=A321516&Location=U2&doc=GetTRDoc.pdf>.

Ölçmen, M.S., Simpson, R.L., 2006. Some structural features of a turbulent wing–body junction vortical flow. Int. J. Heat Fluid Flow 27 (6), 980–993.

Parneix, S., Durbin, P.A., Behnia, M., 1998. Computation of 3D turbulent boundary layers using the v2-f model. Flow Turbul. Combust. 60, 19–46.

Rotta, J.C., 1962. Turbulent boundary layers in incompressible flow. In: Ferri, A., Küchemann, D., Sterne, L.H.G. (Eds.), Progress in Aeronautical Sciences, Boundary Layer Problems, vol. 2. Pergamon Press.

Schwarz, W.R., Bradshaw, P., 1994. Term-by-term tests of stress-transport turbulence models in a three-dimensional boundary layer. Phys. Fluids 6 (2), 986–999.

Shao, L., Le Penven, L., Bertoglio, J.P., 1990. Study of the modelling of the transport terms in one-point closures using large eddy simulation of turbulence. In: Rodi, Ganic (Eds.), Engineering Turbulence Modeling and Experiments. Elsevier Science Publishing Co., Inc., pp. 83–92.

Shih, T.H., Lumley, J.L., Janicka, J., 1987. Second-order modelling of a variable density mixing layer. J. Fluid Mech. 180, 93–116.

Shinpaugh, K.A., Simpson, R.L., 1995. A rapidly scanning two-velocity-component laser Doppler velocimeter. Meas. Sci. Technol. 6, 690–701.

Simpson, R.L., 1996. Aspects of turbulent boundary layer separation. Prog. Aerosp. Sci. 32, 457–521.

Simpson, R.L., 2001. Junction flows. Annu. Rev. Fluid Mech. 33, 415–443.

Speziale, C.G., Gatski, T.B., 1997. Analysis and modeling of anisotropies in the dissipation rate of turbulence. J. Fluid Mech. 344, 155–180.

Sumitani, Y., Kasagi, N., 1995. Direct numerical simulation of turbulent transport with uniform wall injection and suction. AIAA J. 33 (7), 1220–1228.

Sung, Chao-Ho, Yang, Cheng-1, 1988. Validation of turbulent horseshoe vortex flows. In: 17th Symposium on Naval Hydrodynamics, 29 August–2 September, The Hague, Netherlands.

Tagawa, M., Nagano, Y., Tsuji, T., 1991. Turbulence model for the dissipation components of Reynolds stresses. In: 8th Symposium on Turbulent Shear Flows, 9–11/1991, Munich, Germany.